International Journal of Plasticity 148 (2022) 103151

Contents lists available at ScienceDirect

International Journal of Plasticity

journal homepage: www.elsevier.com/locate/ijplas

Transformation plasticity in high strength, ductile ultrafine-grained FeMn alloy processed by heavy ausforming

Qingquan Lai [a,*], Huiqin Yang [a], Yuntao Wei [a], Hao Zhou [b], Lirong Xiao [b], Huiqiang Ying [a], Si Lan [a], Zesheng You [a], Zongde Kou [a], Tao Feng [a], Qi Lu [c], Pascal Jacques [d], Thomas Pardoen [d,*]

[a] Herbert Gleiter Institute of Nanoscience, Nanjing University of Science and Technology, Nanjing 210094, China
[b] Nano- and Heterogeneous Structural Materials Research Center, Nanjing University of Science and Technology, Nanjing 210094, China
[c] China Science Lab, General Motors Global Research and Development, Shanghai 201206, China
[d] Institute of Mechanics, Materials and Civil Engineering, UCLouvain, 1348 Louvain-la-Neuve, Belgium

ARTICLE INFO

Keywords:
Ultrafine-grained materials
Martensitic transformation
Strain hardening
Transformation-induced plasticity
Mechanical properties

ABSTRACT

The mechanisms contributing to the excellent mechanical properties of the ultrafine-grained (UFG) Fe-23 wt.%Mn alloy processed by heavy ausforming are unraveled based on detailed characterization analysis and modelling. The UFG microstructure is fully austenitic after the heavy ausforming step involving a 90% rolling reduction; while the material quenched from the coarse-grained (CG) austenite consists of epsilon (ε)-martensite and austenite. The UFG Fe23Mn alloy shows a high strain-hardening capacity which leads to a much higher true uniform elongation (0.33) and true tensile strength (1330 MPa) than the CG counterpart (0.17 and 950 MPa, respectively). The high ductility of the heavily-ausformed microstructure with no subsequent annealing step contradicts the general trend of UFG alloys produced by severe plastic deformation. In addition, a ductile fracture mode with improved resistance to damage initiation in the UFG microstructure contrasts with the brittleness of the CG counterpart. Therefore, the UFG Fe23Mn alloy exhibits a high combination of strength, resistance to plastic localization and resistance to cracking. This superior mechanical performance is attributed to the gradual deformation-induced ε-martensitic transformation and to the large plastic co-deformation of the UFG ε-martensite, in which twinning is suppressed at the expense of the activation of non-basal <c+a> slip. A mean-field micromechanical model is used to analyze the contribution of the phase transformation to plasticity, and to further rationalize the mechanical response of the UFG ε-martensite. This finding provides new insight into the effects of microstructural scale on the mechanical behavior of this class of transformation-induced plasticity (TRIP)-assisted alloys.

1. Introduction

High-manganese steels are known for their significant strain-hardening capacity and the large uniform elongation, hence constituting promising candidates for numerous applications, such as for automotive structural components and liquid-nitrogen vessels. The deformability of the high-Mn steels is usually attributed to the face-centered cubic (FCC)-hexagonal close-packed (HCP) ε-martensitic

* Corresponding authors.
E-mail addresses: lai@njust.edu.cn (Q. Lai), thomas.pardoen@uclouvain.be (T. Pardoen).

https://doi.org/10.1016/j.ijplas.2021.103151
Received 4 October 2021; Received in revised form 8 November 2021;
Available online 11 November 2021
0749-6419/© 2021 Elsevier Ltd. All rights reserved.

transformation and/or to the mechanical twinning in austenite during deformation, which interplay with the primary dislocation glide mechanism and enhance the strain-hardening rate (Bouaziz et al., 2011; Chowdhury et al., 2017; De Cooman et al., 2018; Grassel et al., 2000).

The transformation-induced plasticity (TRIP) involving ε-martensitic transformation is usually not strictly distinguished from the twinning-induced plasticity (TWIP) (Bouaziz et al., 2011). Both mechanisms occur in austenitic steels with low stacking fault energy (SFE), and the switch from TWIP-dominated to TRIP-dominated deformation occurs when the temperature of deformation is decreased (Allain et al., 2004; Madivala et al., 2018). The ε-martensite forms through the glide of Shockley partial dislocations on every other {111} plane in austenite, while the generation of a twin requires the glide of Shockley partials on every {111} plane (Nishiyama, 1978). These microscopic processes result in a plate-like morphology and an increased density of planar interfaces, leading to a reduction of the dislocation mean free path and to the dynamic Hall-Petch effect (Bouaziz and Guelton, 2001). In addition, the twinned volume and ε-martensite constitute regions stronger than the matrix, which induce a significant kinematic hardening contribution (Gil Sevillano and de las Cuevas, 2019; Sevillano, 2009). However, the high-Mn TRIP steels generally suffer from the brittleness that is associated to the formation of ε-martensite. The premature brittle fracture can be induced by the high stress concentration along ε-martensite/ε-martensite or along ε-martensite/grain boundary interfaces (Koyama et al., 2018, 2012; Wei et al., 2019). In addition, the efficiency of the TRIP effect is also related to the local mechanical response of the constituent phases. The limited ductility of the HCP ε-martensite is a critical issue that sets the final level of mechanical properties reached by high-Mn TRIP steels. In other words, the ε-martensite might not be capable to support large deformations and to bear high stress levels as assumed in the micromechanical models developed for the high-Mn TRIP steels (Liang et al., 2009).

The plasticity of HCP metals, including the ε-martensite, is primarily accommodated by the basal and/or prismatic slip, which involve less than 5 independent slip systems and fail to satisfy the Taylor-von Mises criterion for homogeneous deformation in polycrystalline aggregates. Mechanical twinning and dislocation slip with a <c+a> Burgers vector on the pyramidal planes are activated to accommodate general deformation states (Yoo et al., 2002). Mechanical twinning is a ductilizing vehicle in that it accommodates the strain along the c-axis, but, on the other hand, it can lead to failure due to the accompanying intense local stress concentrations (Christian and Mahajan, 1995; Yoo, 1981). Compared to the strong geometrical constraint on twinning in the HCP structure, the non-basal <c+a> dislocation slip is more efficient in satisfying plastic compatibility (Yoo, 1981). The benefits of activating <c+a> slip have been reported for magnesium (Liu et al., 2019; Wu et al., 2018) and for the FeMn-based high-entropy alloys (Bu et al., 2019; Li et al., 2016), in which the glide of <c+a> dislocations leads to a ductile HCP lattice. Mechanical twinning and non-basal <c+a> slip are competing processes, and the activity of <c+a> dislocations is significantly enhanced when twinning is suppressed in fine-grained or small-sized samples (Koike et al., 2003; Liu et al., 2019; Luo et al., 2020; Zheng et al., 2020). However, more systematic investigations are needed to clarify the mechanical consequences of suppressing twinning in different HCP metals.

Many studies on high-Mn TRIP steels focused on the effect of chemical composition on the microstructure and mechanical properties (Grassel et al., 2000; Koyama et al., 2018; Liang et al., 2009; Pierce et al., 2015). However, there are other metallurgical parameters, which affect the phase constituent responses and deformation mechanisms. For example, grain refinement could suppress martensitic transformation so that less alloying addition is needed to enhance the austenite stability (Nishiyama, 1978). In this sense, heavy ausforming provides a promising solution for exploring the potential of the TRIP steels with more economical composition via the grain size effect. Ausforming is a classical method to improve the mechanical properties of martensitic or bainitic steels (Gong et al., 2013). It was also applied to the FeMn alloys (Sipos et al., 1976; Tomota et al., 1988). Recently, a thin layer of nanograined Fe23Mn microstructure with an average grain size of 70 nm has been processed by surface mechanical treatment at elevated temperature (Lai et al., 2020). The hardness is continuously increased by triggering the phase transformation, demonstrating an unusual strain hardening capacity in the nanograined samples. Therefore, bulk UFG high-Mn steels can be produced by performing an industrially-adaptable ausforming step, taking the advantage of the low austenitization temperature (Nishiyama, 1978). This provides an opportunity to take advantage of the TRIP effect into bulk UFG alloys, the ductility of which is usually low (Pineau et al., 2016). Note that the martensitic transformation and its mechanical consequences in the UFG materials, which involve a strong mechanical constraint by the grain boundaries, remain an open field of investigation (Ko et al., 2017; Waitz et al., 2009). In addition, the UFG ε-martensite is generated by the transformation from an UFG austenite. Considering the challenges for achieving UFG HCP metals by conventional plastic deformation approaches (Cao et al., 2018), the transformation-induced UFG ε-martensite allows for examination of the mechanical behavior of UFG HCP metals and its efficiency as a potential reinforcement of TRIP alloys (Li et al., 2017b; Su et al., 2019).

The present study aims at unravelling the mechanisms contributing to the excellent mechanical properties of the Fe-23 wt.%Mn alloy processed by heavy ausforming, which is accomplished by rolling in the austenitic state with a thickness reduction of 90% to produce bulk UFG microstructure. According to Schuman's map (Schuman, 1972), the FeMn alloys with <26 wt.% Mn are expected to contain some amount of ε-martensite at room temperature. The present Fe23Mn alloy was thus primarily selected to reveal the effects of a heavy ausforming step on the microstructure. The microstructure transformed from coarse-grained (CG) austenite is compared to that from the UFG austenite, in order to determine the grain size effect on austenite stability. In addition, the structural scale of the ε-martensite is also fixed by the austenite grain size, and the impacts of the transformation-induced UFG ε-martensite can be addressed by comparing the deformation and fracture behavior with the CG counterpart. The experimental procedures for the processing, characterization and mechanical testing are described in Section 2. The experimental results are presented in Section 3. The microstructure engineering by heavy ausforming, the deformation and strengthening mechanisms in the UFG microstructure are discussed in-depth in Section 4, followed by the conclusions in Section 5. The outcomes of this study are expected to open up another pathway for the development of strong-and-ductile metastable alloys by engineering the prior austenitic microstructure.

2. Experimental procedures

The Fe-23 wt.%Mn and Fe-30 wt.%Mn alloys were produced by vacuum induction melting and casting. The carbon content of the Fe23Mn and Fe30Mn alloys are equal to 0.006 wt.% and 0.009 wt.%, respectively. The ingots were homogenized at 1000 °C for 24 h under Ar atmosphere. After hot forging, the alloys were annealed at 1000 °C for 1 h and subsequently air quenched, the as-quenched microstructure being transformed from the coarse-grained austenite. The phase transformation during heating and cooling of the CG Fe23Mn alloy was studied by quenching dilatometry (DIL 805A/D). The sample with dimension 10 mm × 4 mm × 2 mm was heated from room temperature (RT) at the rate of 30 °C /s in He flux. When heated to 900 °C, the sample was held for 20 min and cooled at 30 °C /s to RT. The austenite start (A_s) and finish (A_f) temperatures and the ε-martensite start temperature (E_s) were determined by monitoring the change of sample dimensions during the thermal cycle.

The ausforming temperature was determined according to the dilatometry measurements so as to guarantee a fully austenitic state during rolling. The plates of Fe23Mn alloy with 18 mm thickness and 30 mm width were kept at the ausforming temperature for 30 min and subjected to rolling. The temperature of the sample right after rolling was above 300 °C as measured by infrared thermometer. A 90% thickness reduction was imposed through 10 passes. After each pass, the plates were re-heated for 5 min. The 90% rolling reduction corresponds to an equivalent true plastic strain of 2.66 according to

$$\varepsilon^{eq} = -\frac{2}{\sqrt{3}}\ln\left(\frac{t_f}{t_0}\right) \tag{1}$$

where t_f and t_0 are the final and initial thickness, respectively.

Metallographic preparation can induce martensitic transformation at the surface layer in the Fe23Mn alloy, as proven by careful microstructure examination (Fig. S1). In order to characterize the true microstructural state of the bulk samples, neutron diffraction experiments were carried out using a deep-penetrating neutron beam with high intensity and good spatial resolution on a General Purpose Powder Diffractometer with a 360 ° rotation stage at the China Spallation Neutron Source. The power of the neutron source was 100 kW. The time-of-flight method was used to collect data over a total scanning time of 2 h. The volume fraction of ε-martensite is determined by the method of Rietveld refinement. The peak broadening of the profiles is also characterized by the Williamson-Hall Method (Ungar, 2001). These results thus provided also a reference set of data to assess the possible artifacts from sample surface preparation.

The samples for characterization were cut along the plane parallel to the rolling (RD) and normal (ND) directions. After grinding and mechanical polishing down to 1 μm, the preparation was followed by colloidal silica polishing for 90 min and finished by the ion-beam treatment using Leica TIC3X (details shown in Fig. S2). The microstructures were characterized by electron backscatter diffraction (EBSD), at an acceleration voltage of 20 KV and a 50 nm step size. The information on phase constituents and local orientation was analyzed with the HKL Tango software. The active twin types in the HCP phase were identified using the boundary misorientation axis-angle relationship. The $\{10\bar{1}2\}$ extension twin boundaries were determined by a misorientation of $86° \pm 5°$ around

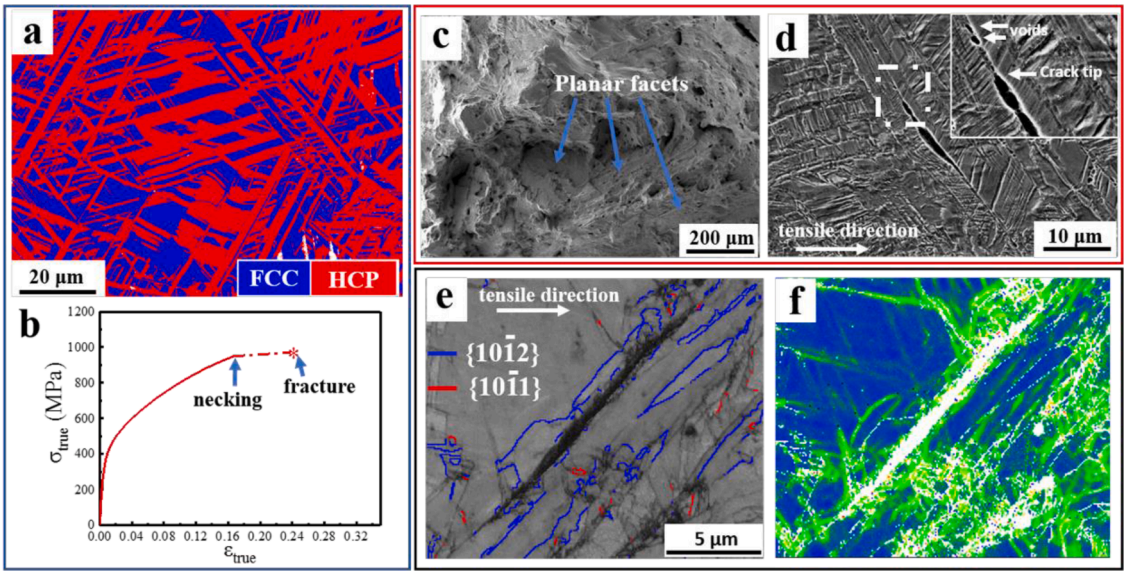

Fig. 1. (a) The microstructure of the CG Fe23Mn alloy attained by EBSD. (b) True stress-strain response. A linear extension from necking is made to indicate the fracture strain and fracture stress. (c) Fracture surface of the broken specimen of the CG Fe23Mn and (d) the SEM micrographs on the cross-section showing the damage mechanisms. (e) Identification of twins around a microcrack, with blue lines indicating the $\{10\bar{1}2\}$ twin and the red lines indicating the $\{10\bar{1}1\}$ twin and (f) the distribution of local misorientation; (e) and (f) are obtained by EBSD. (For interpretation of the references to colour in this figure legend, the reader is referred to the web version of this article.)

the axis of $\langle 11\bar{2}0\rangle$, and the $\{10\bar{1}1\}$ contraction twin boundary was associated to a misorientation of 55°± 5°around $\langle 11\bar{2}0\rangle$. The distribution of local misorientation was plotted with a 5 × 5 filter size and a subgrain angle of 5°. The morphology was observed by scanning electron microscopy (SEM) after 10% Nital etching. Thin-film specimens were prepared with the twin-jet electropolishing at 20 V in a 10% $HClO_4$ acetic acid electrolyte, and observed by transmission electron microscopy (TEM) (FEI Tecnai 20). The high-resolution analysis was conducted on an aberration-corrected TEM (Titan G2 60–300) operated at 300 kV.

The mechanical properties were measured by monotonic uniaxial tensile testing at an engineering strain rate of 10^{-3} /s. The materials were cut into dog-bone shaped specimens with the longitudinal direction along RD with a 2 mm width and a 5 mm gauge length. The strain in the gauge section was measured by using the home-made digital image correlation system, details seen in Wang et al. (2018). The fracture surface of the broken tensile specimens was observed by SEM. The fracture surface area (A_c) was measured by combining laser scanning confocal microscopy (Olympus LEXT) and the software LEXT-OLS4. The true fracture strain ε_f is determined from

$$\varepsilon_f = \ln\frac{A_0}{A_c} \tag{2}$$

where A_0 is the initial cross-section area. The true macroscopic tensile fracture stress is determined by dividing the load at fracture by A_c. Hereafter, the broken tensile specimens were cut along the central axis, and the damage observation was made on the rolling plane close to the fracture surface.

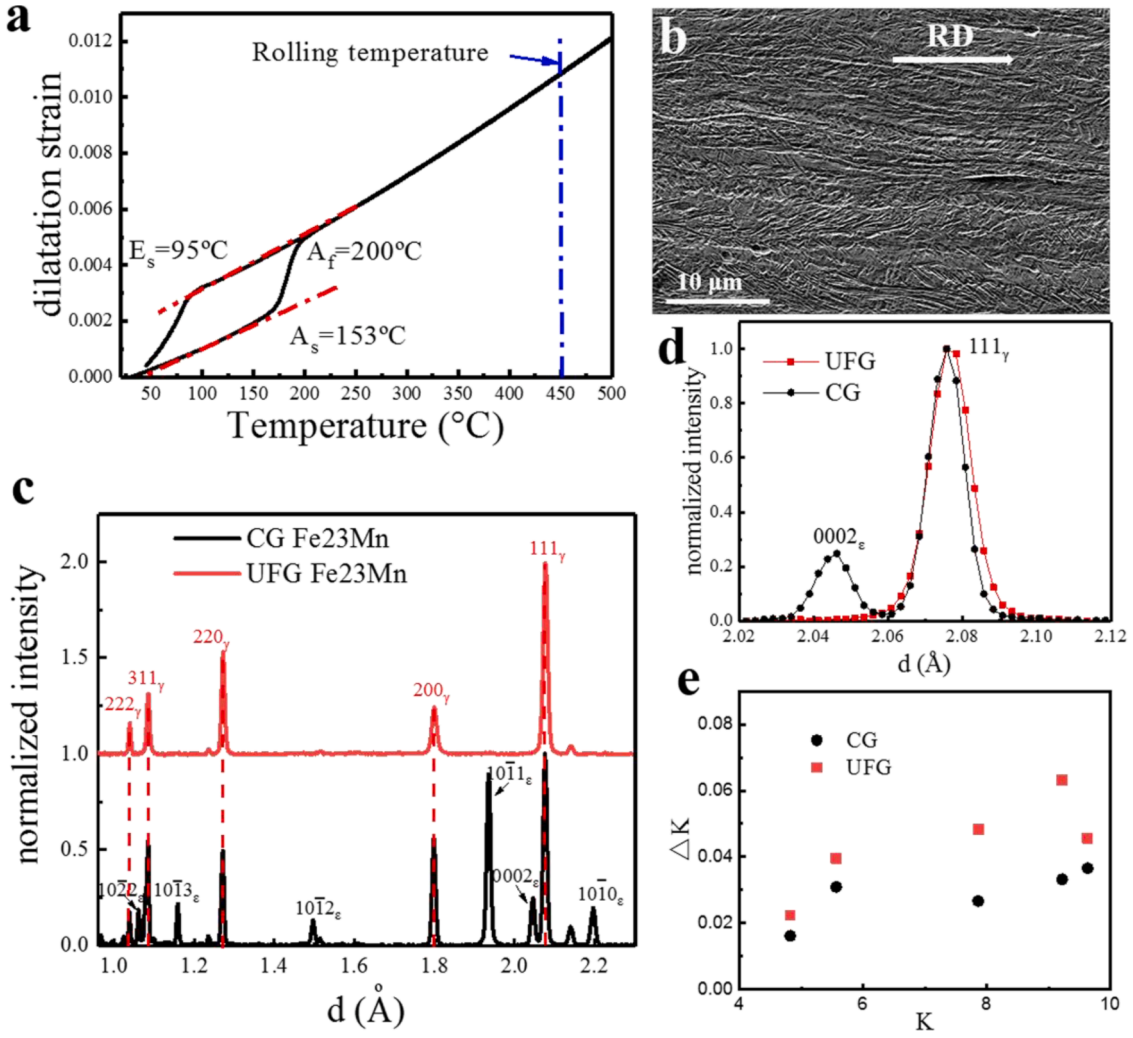

Fig. 2. (a) Dilatometry response of the CG Fe23Mn during a heating-cooling cycle; (b) SEM micrograph of the heavily-ausformed microstructure. (c) The neutron diffraction results with the peaks being indexed, and (d) is the zoom-in for selected peaks. The intensities in (c) and (d) were normalized by that of $\{111\}_\gamma$. (e) Williamson-Hall plots of the UFG and CG Fe23Mn samples.

3. Experimental results

The microstructure of the CG Fe23Mn alloy is shown in Fig. 1a, exhibiting the plate-type morphology of the ε-martensite which subdivides the prior austenite grains. The volume fraction of ε-martensite is equal to 60 vol.%. Fig. 1b shows the true stress-true strain response of the CG microstructure. The true uniform elongation and true fracture strain are equal to 0.17 and 0.24, respectively, indicating limited post-necking deformation. Note that a fracture strain equal to 0.24 is a small value for a steel with such a moderate tensile strength. The tensile fracture stress (980 MPa) is slightly higher than the true tensile strength (947 MPa), but it is still lower than the tensile strength of many conventional high-strength steel grades. The magnitude of such macroscopic fracture stress is also very low when one considers the strong atomic bond of iron. Large planar facets are frequently observed on the fracture surface of the broken specimen (Fig. 1c). The planar facets on the fracture surface correspond to the cracking along the boundary between ε-martensite plates, as shown in Fig. 1d. The cracks propagate along the boundary by the formation and coalescence of microvoids ahead of the crack tip. This probably results in the very small dimples within the planar facets on the fracture surface. EBSD mapping around a microcrack reveals a large amount of $\{10\bar{1}2\}$ twins (Fig. 1e) and significant misorientations (Fig. 1f), implying that microcracking is induced by twinning and a localized deformation process.

The Fe23Mn alloy was then engineered via heavy ausforming, and the processing parameters were guided by the dilatometry measurements. Although both the austenite and ε-martensite are compact phases, there is a slight volume change during the transformation with detectable dilatation, as shown in Fig. 2a. The A_s (153 °C), A_f (200 °C) and E_s (95 °C) agree well with previously published experimental data and empirical predictions in Nakano and Jacques (2010). The ausforming temperature was thus set equal to 450 °C. The heavily-ausformed microstructure is shown in Fig. 2b, being characterized by an ultrafine and pancaked morphology along RD. The non-metallic inclusions were also significantly elongated. The neutron diffraction results in Fig. 2c show that, the ausformed sample only involves a single-phase FCC structure; while the CG state consists of 65 vol.% of ε-martensite, which is close to the measurement by EBSD. The suppression of ε-martensitic transformation in the ausformed sample is also clearly shown in Fig. 2d. The microstrain resulting from the storage of dislocations in the UFG sample is determined by the classical Williamson-Hall procedure. As shown in Fig. 2e, the full width at half maximum $\triangle$K is plotted as a function of $K=1/d_{hkl}$, where d_{hkl} is the interplanar spacing. The magnitude of the microstrain is evidenced by the more rapid increase of $\triangle$K with K in the UFG sample when comparing with that of the CG sample.

As shown in Fig. 3a, the heavily-ausformed Fe23Mn sample involves a fully-austenitic UFG microstructure, associated with a high density of high-angle grain boundaries (HAGBs) and low-angle grain boundaries (LAGBs). The austenite stability is thus mechanically enhanced through heavy ausforming. The enlarged micrographs of the selected area show that the HAGBs in the austenite are generally aligned along the RD and result in a UFG pancaked structure. Microscopic details of the ausformed sample are provided by the TEM observations. Fig. 3b shows the ultrafine pancaked grains with an average thickness of 220 nm. The austenite grains are highly dislocated with a distribution of extended SFs as shown in Fig. 3c. Fig. 3d and 3e are local observations of the SFs, which are confirmed by the streaking lines in the inserted Fast Fourier Transformation (FFT) patterns. The difference in the width of SFs could be induced by

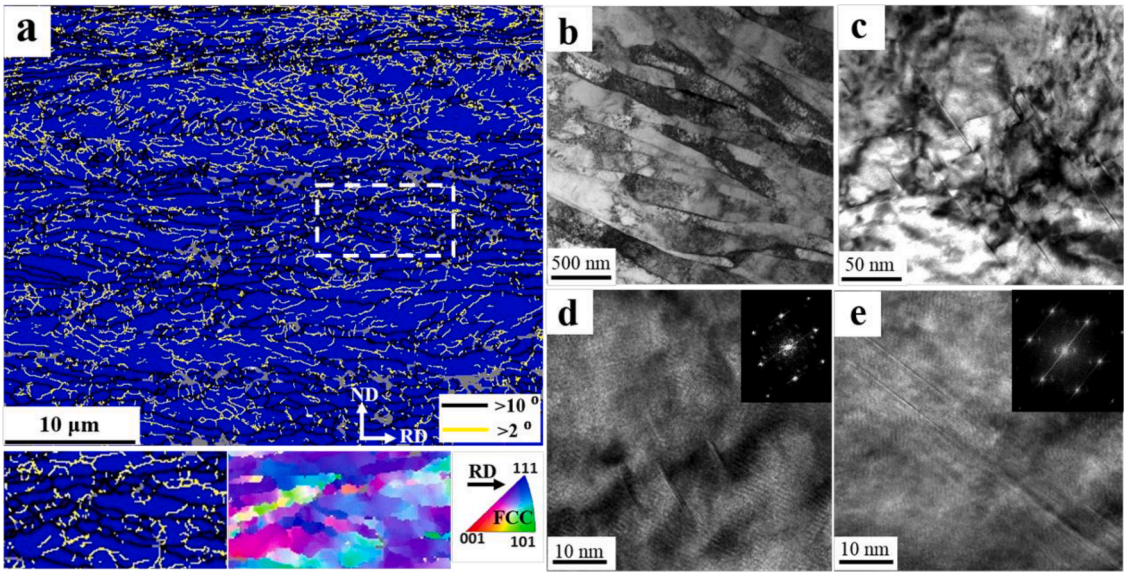

Fig. 3. Characterization of the heavily-ausformed Fe23Mn alloy. (a) The austenitic microstructure (in blue) superimposed with the HAGBs (>10°) and LAGBs (<2°), of which the LAGBs and HAGBs are indicated by yellow and black lines, respectively; the phase map and Inverse Pole Figure (IPF) of the selected area are magnified. (b) Bright field (BF) TEM image showing the heavily-ausformed microstructure; (c) magnified micrograph with a high density of SFs; (d) and (e) are the HR-TEM observation of the SFs. (For interpretation of the references to colour in this figure legend, the reader is referred to the web version of this article.)

the distribution of internal stresses. These microstructural observations consistently demonstrate that the UFG Fe23Mn alloy with fully austenitic microstructure was successfully generated by heavy ausforming. The ε-martensitic transformation during cooling to RT was fully suppressed in the UFG microstructure, although there are plenty of SFs which are potential nucleating defects for ε-martensite. Additional characterizations were performed to confirm the homogeneity of the ausformed sample, details of which are provided in Fig. S3.

The uniaxial tensile responses of the CG, UFG Fe23Mn and CG Fe30Mn alloys are compared in Fig. 4. The Fe30Mn alloy is within the composition regime for a fully austenitic microstructure at RT (Schuman, 1972), involving the lowest yield strength (163 MPa) but the largest ductility ($\varepsilon_u = 0.4$). The higher strength level of the CG Fe23Mn alloy compared to CG Fe30Mn is due to the strengthening by ε-martensite and by the smaller austenite regions subdivided by the ε-martensite plates (Fig. 1a). The UFG Fe23Mn presents a higher yield strength (480 MPa) than the CG counterpart (260 MPa), with simultaneous enhancement of the true tensile strength (1330 MPa) and true uniform elongation (0.33). Contrarily to the limited ductility usually observed in UFG metals right after intense plastic forming, the ausformed UFG Fe23Mn alloy exhibits a high strength-ductility combination without the need of a subsequent annealing step.

The plastic deformation of the Fe30Mn alloy is associated with the formation of dislocation cells and the ε-martensitic transformation is hardly triggered during tensile testing (Liang et al., 2009). Therefore, the CG Fe30Mn sample presents a typical stage-III strain hardening behavior (Fig. 4b). The CG Fe23Mn presents a high initial strain-hardening rate, which dramatically decreases during deformation, leading to early onset of necking as predicted by the Considère criterion. As a comparison, the strain-hardening rate of the ausformed UFG Fe23Mn, which is also high at small deformation, decreases in a more gradual manner, so that necking is postponed to a much larger strain. The postponed necking is also explained by a high strain hardening exponent at large strain, as shown in the Supplementary Fig. S4. The increase of the HCP volume fraction continues to a large extent during tensile deformation of the UFG Fe23Mn; while the occurrence of deformation-induced transformation in the CG sample is much smaller (Fig. 4c). Note that Fe23Mn is beyond the composition regime in which BCC α'-martensite can appear upon straining (Schuman, 1972). The negligible formation of strain-induced α'-martensite is proven by magnetic measurements (see Supplementary Fig. S5).

The microstructural evolution during tensile deformation was characterized in order to establish the structure-property relationship and to elucidate the origin of the superior mechanical properties of the UFG Fe23Mn alloy. Fig. 5a presents the microstructure

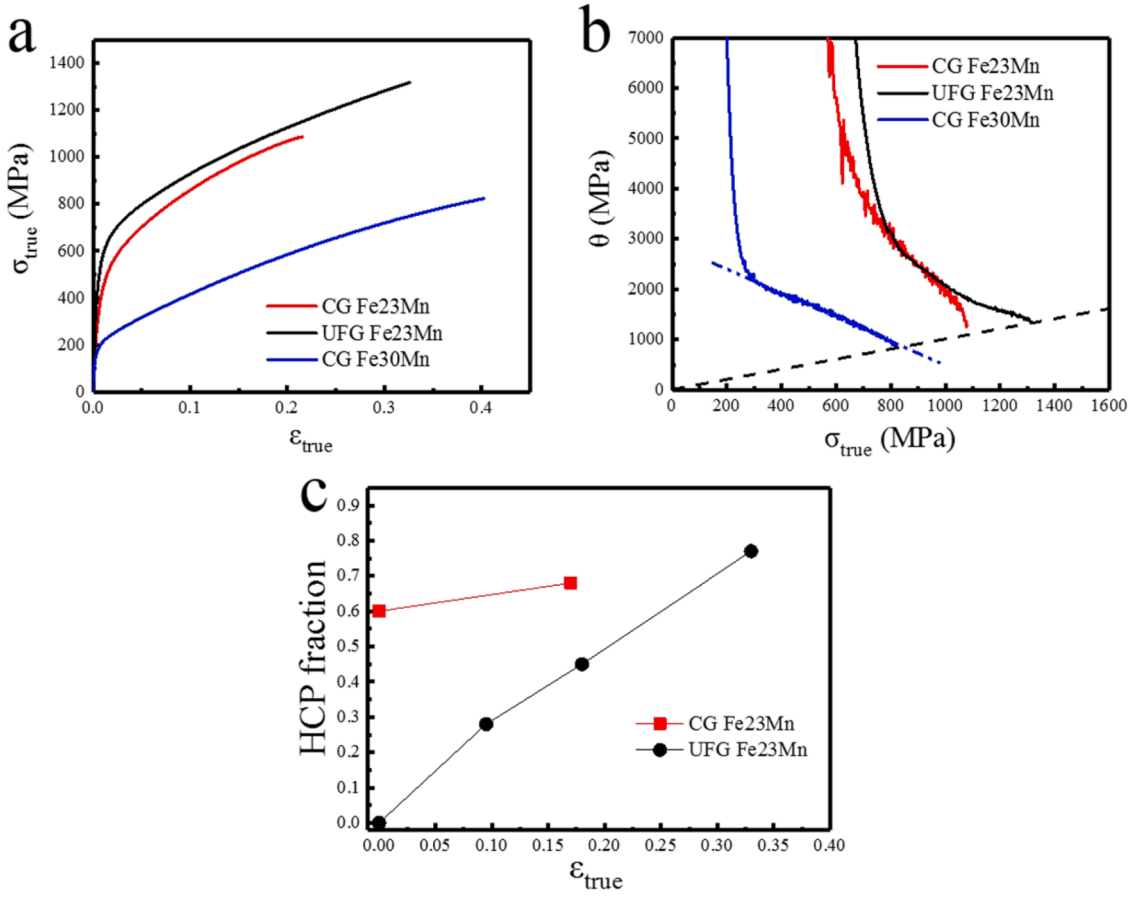

Fig. 4. (a) True stress-strain curves of the CG and UFG Fe23Mn alloy and the CG Fe-30Mn alloy; (b) evolution of strain hardening rate (θ) with true stress; (c) evolution of HCP volume fraction in the CG and UFG Fe23Mn alloy obtained by EBSD.

after a deformation $\varepsilon_{true} = 0.10$. ε-martensite with 28 vol.% has been formed at this stage, distributed either at the prior pancaked austenite grains or along the deformation bands with an inclined angle of ~45°. The detailed observations in Fig. 5b show the lamellar morphology of the ε-martensite, while no ε-martensite intersections and grain subdivision are observed in contrast with the CG state in Fig. 1a. In addition, different orientations of ε-martensite are formed within the individual deformation bands that go through the grain boundaries. Fig. 5c shows that the LAGBs in the prior austenite grains can either induce the nucleation of ε-martensitic transformation or impede the transformation fronts, but when the ε-martensite crosses the LAGBs, the latter will be inherited and constitutes the substructures in the newly-formed ε-martensite.

As the tensile strain is increased up to necking, the ε-martensite becomes the major constituent in the microstructure (Fig. 6a). The generation of dislocation substructures in ε-martensite, which is an indicator of plastic co-deformation, can also be characterized by the development of a local misorientation as shown in Fig. 6b. The prior pancaked austenitic grains are mostly transformed into the pancaked HCP grains, each grain involving almost a single variant of ε-martensite along the thickness direction of the lamellar (Fig. 6c). No mechanical twinning can be identified in the austenite, and mechanical twinning in the ε-martensite is also largely suppressed with only small amount of detected twin boundary segments (Fig. 6d).

The TEM observations in Fig. 7 provide more details about the strain-induced transformation products. Fig. 7a is the overview of the microstructure of the UFGs with a high density of planar defects. Magnified micrographs show that the microstructure consists of either the faulted HCP phase (Fig. 7b) or the FCC + HCP mixture (Fig. 7c), according to the accompanying diffraction patterns. The ε-martensite exhibits the Nishiyama orientation relationship with the austenite (Nishiyama, 1978):

$$\left(1\bar{1}1\right)_{fcc} // \left(0001\right)_{hcp} \tag{3a}$$

$$\left[01\bar{1}\right]_{fcc} // \left[11\bar{2}0\right]_{hcp} \tag{3b}$$

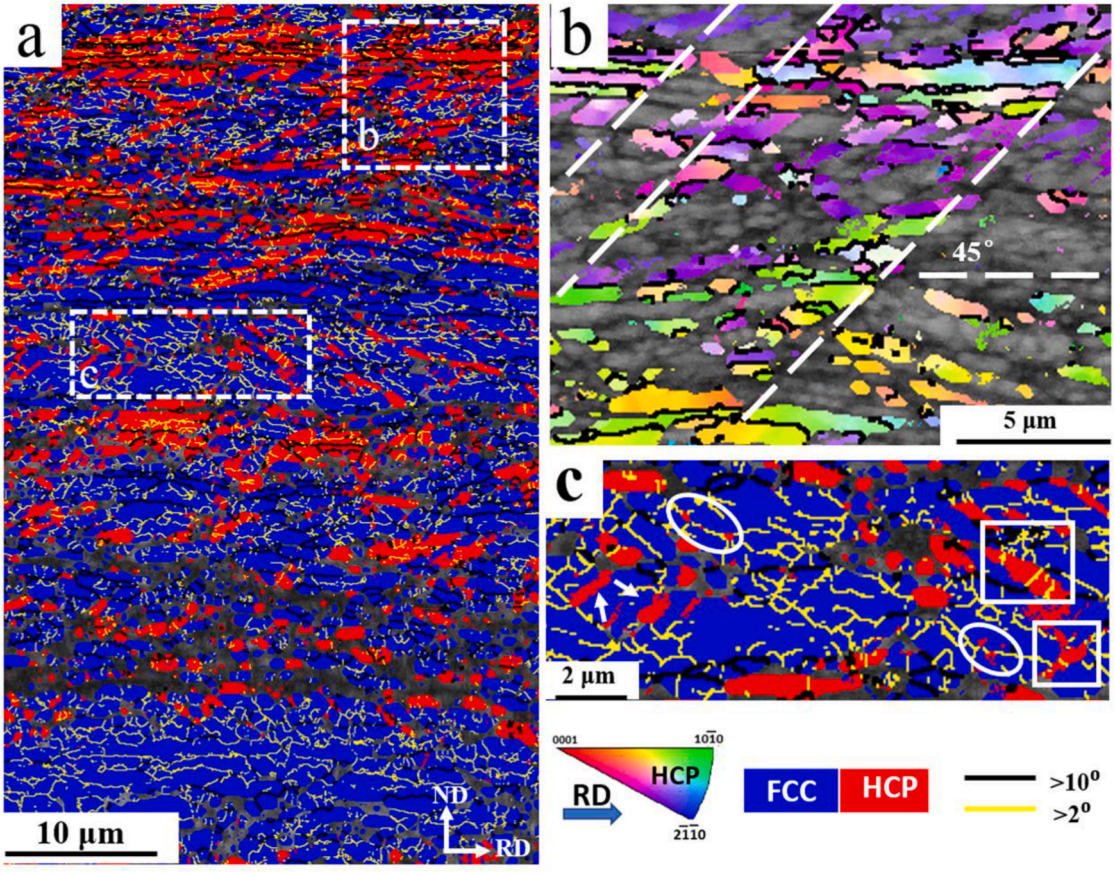

Fig. 5. EBSD characterization of the UFG Fe23Mn after tension to $\varepsilon_{true} = 0.10$. (a) Phase mapping, in which the blue and red areas correspond to the FCC and HCP phases, respectively. The HAGBs and LAGBs are both superimposed on the FCC and HCP phases, which are indicated by black and yellow lines, respectively. (b) The Inverse Pole Figure (IPF) of HCP phase with the superimposed HAGBs and (c) the distribution of phase constituents and grain boundaries in the selected areas. In (c), the nucleation events are marked by circles; the arresting of transformation fronts is indicated by arrows; the inheritance of LAGBs by transformation is highlighted by square boxes. (For interpretation of the references to colour in this figure legend, the reader is referred to the web version of this article.)

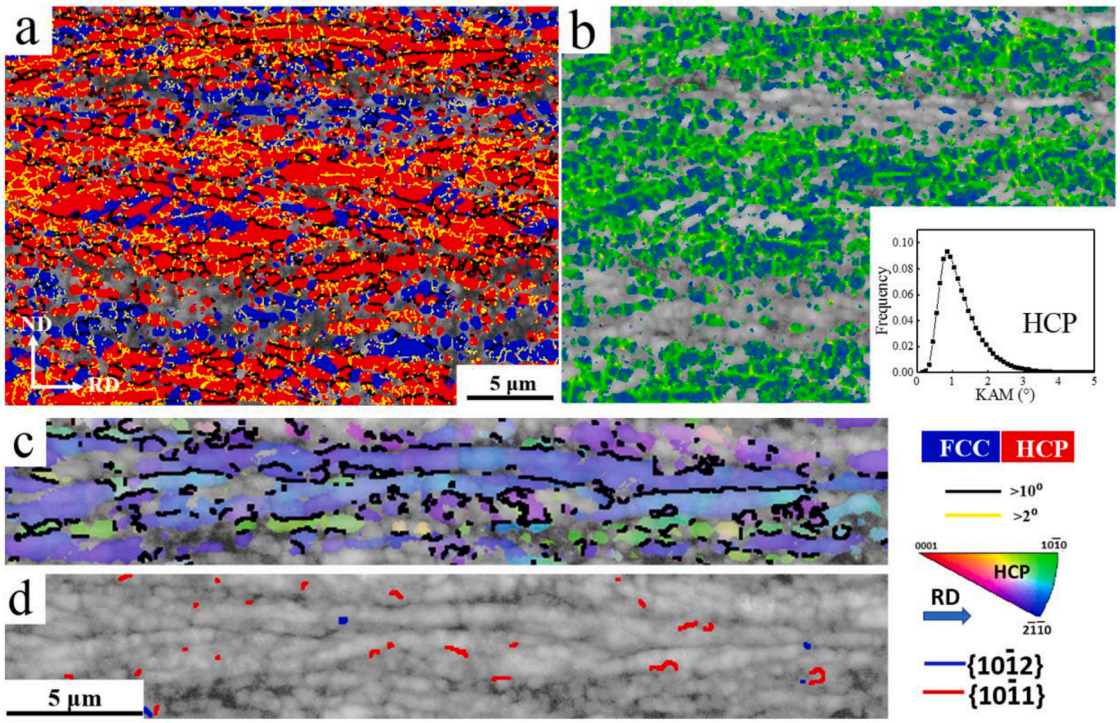

Fig. 6. EBSD characterization of the UFG Fe23Mn after tension to $\varepsilon_{true} = 0.33$. (a) Phase mapping, in which the blue and red areas correspond to the FCC and HCP phases, respectively. The HAGBs and LAGBs are both superimposed on the FCC and HCP phases, which are indicated by black and yellow lines, respectively. (b) The distribution of local misorientation of the same area. (c) The IPF of HCP phase with the distribution of HAGBs and (d) the distribution of $\{10\bar{1}2\}$ and $\{10\bar{1}1\}$ twin boundaries at the same selected area, which are superimposed to the band contrast. (For interpretation of the references to colour in this figure legend, the reader is referred to the web version of this article.)

Consistent with the EBSD results in Fig. 6, it is difficult to identify features of twinning in ε-martensite by using TEM. One of the very few indications of twinning is captured in Fig. 7d, confirmed by the inserted diffraction pattern. This diffraction pattern consists of two sets of HCP spots, as well as one set of FCC spots. The two sets of HCP spots correspond to a classic $\{10\bar{1}2\}$ twinning orientation relationship, while one set of HCP spots has the Nishiyama orientation relationship with the FCC spots. Therefore, the matrix is constituted by the HCP + FCC mixture, as well as by the high-density SFs characterized by the streaking lines in the diffraction pattern. Within this matrix region of 200 nm in size, the $\{10\bar{1}2\}$ twins nucleate from the GB, but their growth is impeded by the SFs and by the retained austenite domain.

The HR-TEM micrograph in Fig. 7e shows a highly-faulted region with both FCC and HCP phases, involving only one variant of transformation. The zoom-in of the selected area shows that parallel SFs are formed adjacent to the HCP plate, which suggests that the generation of SFs is not a limiting step of the transformation. Hence, the deformation-induced ε-martensitic transformation could proceed through the gradual overlapping of SFs. In addition, the propagation of SFs along another slip system (arrowed) is prohibited by the existing SFs with small spacing. Fig. 7f_1 is the HR-TEM observation of the ε-martensite. The HCP structure involves s high density of SFs. In addition, the storage of both <a> and <a+c> type dislocations is identified by drawing the Burgers circuit, with the Burgers vectors schematically shown in the HCP lattice in Fig. 7f_2.

The dislocation structure in the deformed UFG ε-martensite was studied by the TEM two-beam analysis. The observed area involves only the HCP diffraction spots. Fig. 8 presents the results of the two-beam analysis using three different diffraction conditions near the $[11\bar{2}0]$ zone axis. The diffraction condition with $g = [0002]$ makes the dislocations containing a <c> component clearly visible (Fig. 8a), which are either <c+a> dislocations with $b = 1/3[1\bar{2}13]$ or <c> dislocations with $b = [0001]$ according to the $g*b = 0$ invisibility condition (Kim and De Cooman, 2017). The <a> dislocations with $b = 1/3[11\bar{2}0]$ satisfy the visibility criterion with the two-beam conditions in Fig. 8b and 8c, as well as the SFs. Fig. 8a shows that non-basal slip is highly activated, and the dislocations with a <c> component are mostly short segments with small spacing. The proportion of dislocations both visible under $g = [0002]$ and $g = [1\bar{1}00]$ are <c+a> dislocations, while those visible under $g = [0002]$ but invisible under $g = [1\bar{1}00]$ are <c> dislocations. Although <c> dislocations are known as sessile dislocations (Jones and Hutchinson, 1981; Wu and Curtin, 2016), the zoom-in of Fig. 8d shows a high density of <c> dislocations. These <c> dislocations are organized into a wall that accommodates the local misorientation, which might correspond to the LAGBs shown in Fig. 6. Therefore, the deformation in the UFG ε-martensite is accommodated by the activation of non-basal slip of dislocations with a <c> component, in contrast with the twinning mechanism dominating in the CG counterpart.

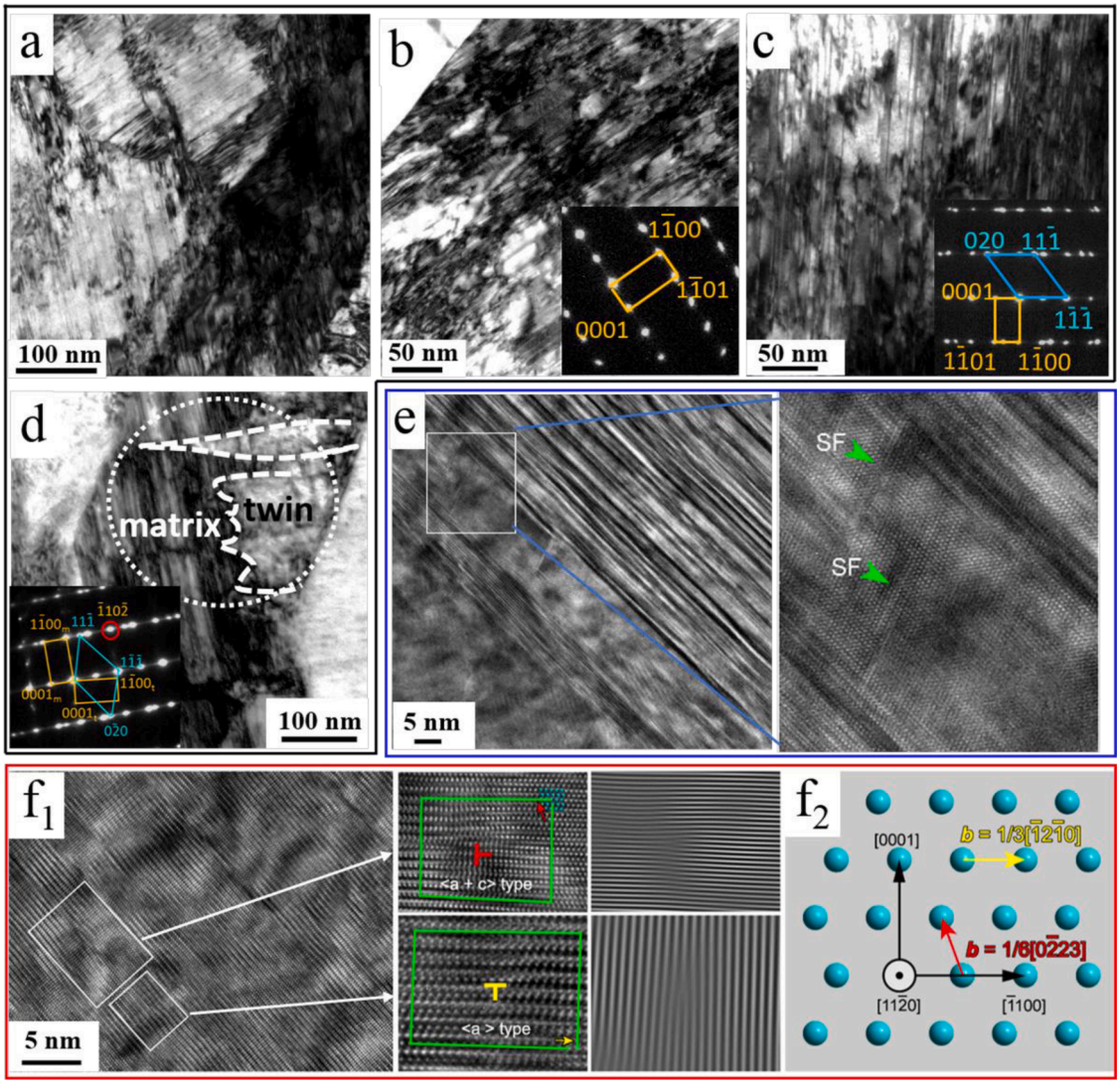

Fig. 7. Microscopic observations of the UFG microstructure after tension to $\varepsilon_{true} = 0.33$. (a) TEM BF micrograph showing the high density of planar defects in the ultrafine grains; (b) and (c) local areas within HCP phase and FCC + HCP mixture, respectively; (d) a twinning event captured in an ultrafine grain, with the corresponding diffraction pattern. (e) High-resolution TEM micrograph within a region containing both HCP and FCC phases, associating with a zoom-in image which shows the intersection of stacking faults in the FCC phase. (f1) The HR-TEM of ε-martensite with atomic resolution zooms to shows the dislocations with the Burger's circuits; (f2) showing the Burgers vector in a schematic illustration of the HCP lattice projected along the $[11\bar{2}0]$ axis.

The above EBSD and TEM observations demonstrate that the UFG ε-martensite can deform plastically without twinning. Although both the CG and UFG Fe23Mn samples involve a similar HCP volume fraction at failure, the tensile fracture stress of the UFG Fe23Mn sample (1520 MPa) is much higher than the CG one (980 MPa). The true fracture strain of the heavily-ausformed sample (0.49) is also much higher than the CG counterpart (0.24). The high fracture strain comes both from high uniform deformation and reasonable post-necking deformation as shown in Fig. 9a. The UFG Fe23Mn sample exhibits a fracture surface covered by dimples, implying a ductile fracture mode (Fig. 9b and 9c). Two populations of dimples are uniformly distributed, the larger ones with a mean size of 4.8 ± 2.0 μm (average of 10 dimples) and the smaller one of 1.4 ± 0.6 μm (average of 100 dimples) (Fig. 9b). A detailed observation in Fig. 9c indicates a final instability by a shear failure mode. The damage analysis on the sectioned surface (Fig. 9d–f) is consistent with the observation made on the fracture surface. The fracture surface is orientated at 39° with respect to the tensile direction (Fig. 9d), indicating the development of a shear fracture mode within the necking region. The typical damage accumulation associated to large voids and/or microcracks is not really observed below the fracture surface. Small amount of micron- and submicron-sized voids are identified with an equiaxed shape (Fig. 9e and 9f). The coalescence of microvoids involving submicron-sized voids in the ligament is captured in Fig. 9e. The submicron voids can also be found uniformly distributed in the matrix (Fig. 9f). In summary, the UFG Fe23Mn alloy fails in a ductile manner, overcoming the intrinsic brittleness of the HCP phase. Since the dimple size is close to the void size, the

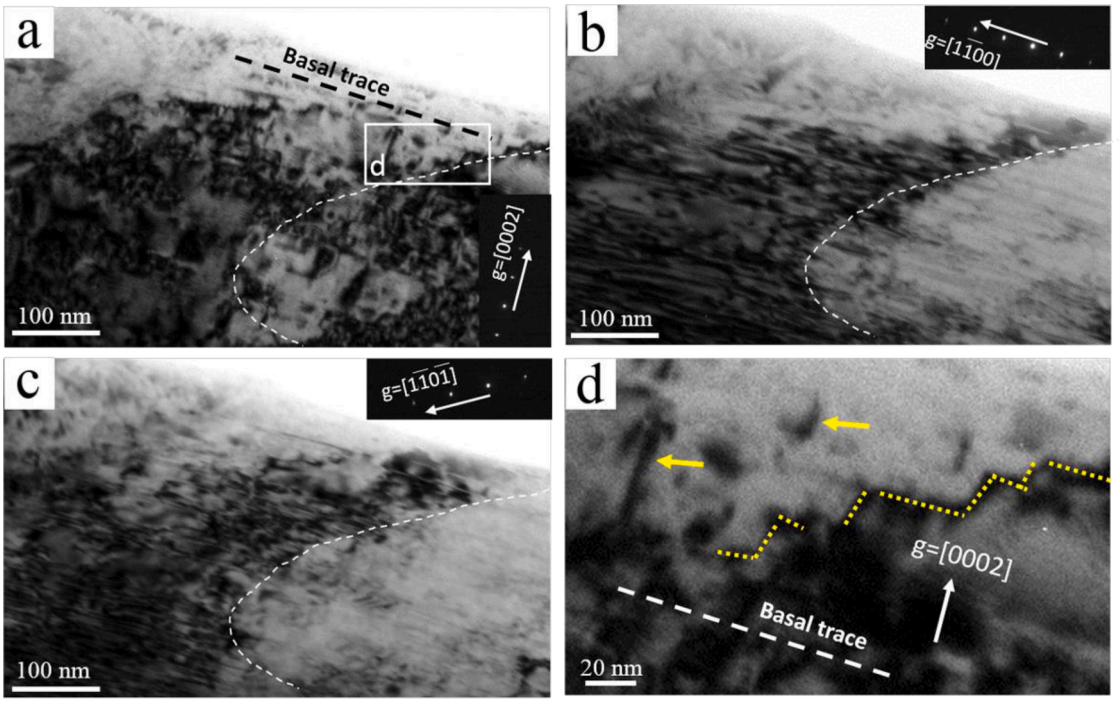

Fig. 8. Bright-field images of the two-beam analysis near the $[11\bar{2}0]$ zone axis of HCP phase using the diffraction condition of [0002] (a), $[1\bar{1}00]$ (b) and $[1\bar{1}01]$ (c), respectively; (d) is a zoom-in taken from (a), showing the organization of the dislocations. The dotted white lines in (a) to (c) indicate the location of a LAGB. The dotted yellow lines and arrows in (d) highlight the segments of <c> dislocations. (For interpretation of the references to colour in this figure legend, the reader is referred to the web version of this article.)

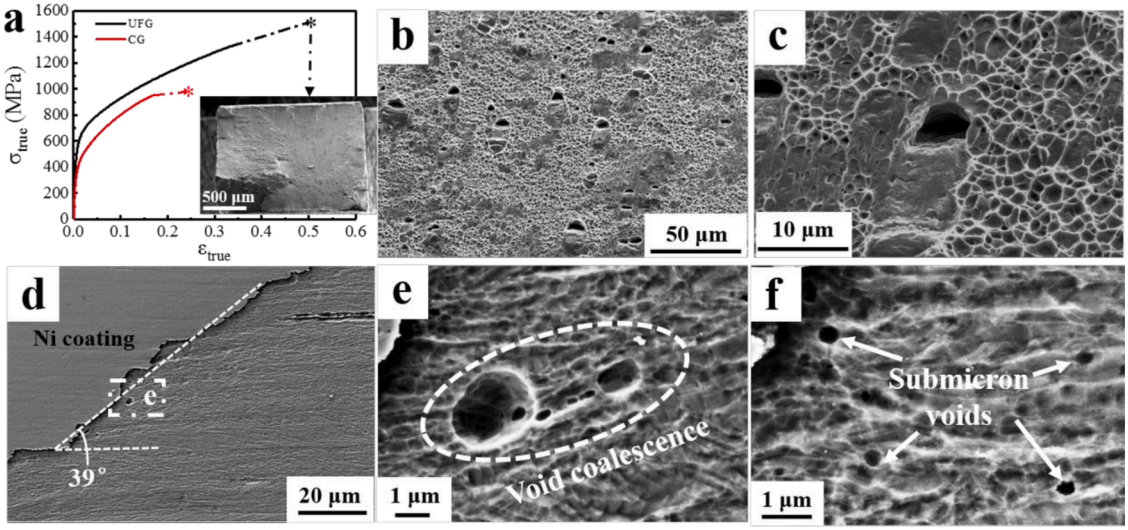

Fig. 9. Characterization of the fracture and damage behavior of the heavily-ausformed Fe23Mn alloy. (a) The true stress-strain curve extending to fracture, the overview of fracture surface being inserted; (b) and (c) micrographs of fracture surface at different magnifications. (d)–(f) Micrographs taken on the sectioned sample near the fracture surface.

void growth stage during ductile fracture is limited and the fracture appears thus to be dominated by the damage nucleation process. The final instability is not dictated by the necking of ligaments between primary voids, but is determined by the nucleation and coalescence of small secondary voids which quickly follow the formation of primary micro-sized voids (Fabregue and Pardoen, 2008).

4. Discussion

4.1. Microstructure engineering by heavy ausforming

Deformation-induced grain refinement is accomplished by dislocation storage and organization into new GBs, which involves a competition between dislocation multiplication and dynamic recovery. Dynamic recovery is a thermally activated process, and a lower deformation temperature mitigates dynamic recovery mechanisms, leading to more efficient grain refinement (Cao et al., 2018). The low A_f temperature (200 °C) of the Fe23Mn alloy leads to a moderate ausforming temperature, and the rolling process successfully induces a bulk UFG material as shown in Fig. 3. The pancaked austenite grains indicate limited recrystallization. The grain refinement of Fe23Mn alloy during ausforming was even pushed down to the nanocrystalline regime (<100 nm) via surface mechanical treatment in a preliminary study (Lai et al., 2020).

Prior deformation and grain refinement cooperate to enhance the austenite stability (Nishiyama, 1978; Takaki et al., 1993; Tsuzaki et al., 1991; Waitz et al., 2009). For the high-Mn Fe alloys that undergo ε-martensitic transformation, a moderate austenite pre-deformation was found sufficient to suppress the thermal transformation. The study in Tsuzaki et al. (1991) showed that 40% austenite pre-deformation of the Fe24Mn alloy at 400 °C fully stabilizes the austenite to RT; while the results in Tomota et al. (1988) indicate the existence of a threshold rolling reduction by 30% at 400 °C on the Fe25Mn alloy. The feasibility to fully suppress the thermal ε-martensitic transformation in the FeMn alloy systems can be explained by a thermodynamic argument. The ε-martensitic transformation is treated as a faulting process on closest-packed planes, the faulting energy involving the chemical free energy, volume strain energy and interfacial energy contributions, and the transformation propagates by the motion of an array of Shockley partials at the FCC/HCP interface (Olson and Cohen, 1976). The $(111)_\gamma$ plane is the habit plane due to the small distortion accompanying the transformation, and the interface is coherent (Howe et al., 2009; Nishiyama, 1978).The driving force is related to the Gibbs free energy change due to structure change, while the resistance forces include the interfacial energy, the strain energy and the obstacles to the motion of interfacial dislocations. The FCC—HCP transformation in the FeMn binary alloys is associated with a small Gibbs energy change, e.g. ~260 J/mole in the Fe23Mn alloy (Nakano and Jacques, 2010). This indicates that the resistance force to suppress the thermal ε-martensitic transformation will be moderate, and can possibly be provided by the forest dislocations, which inhibit the motion of the dislocations at the propagating interface.

The present UFG Fe23Mn alloy processed by 90% ausforming involves a fully austenitic microstructure at RT (Figs. 2 and 3). Since this alloy composition is similar to the above-mentioned earlier studies, a moderate austenite pre-deformation is presumably sufficient to fully suppress the thermal ε-martensitic transformation. Note that the abundant rolling deformation generates the dislocation substructure, which provides the potent nucleation sites for martensitic transformation (Olson and Cohen, 1976). Actually, according to the observations in Fig. 3, the dislocations in the ausformed sample are often dissociated into stacking faults, each stacking fault being considered as a platelet of HCP of a thickness of two atomic layers, i.e. a HCP embryo. Therefore, the major impact of the dislocation substructure in the UFG Fe23Mn alloy is, instead of enhancing the nucleation rate by providing numerous embryos, to impede the transformation by generating the obstacles (GBs and dislocations) to the motion of interfacial dislocations, which is an effect of mechanical stabilization overwhelming the chemical driving force.

4.2. Transformation mechanism of the UFG Fe23Mn alloy

The multiplication of SFs and ε-martensitic transformation significantly contribute to the plastic deformation of the ausformed UFG microstructure. The planar slip character is explained by the low SFE ≈ 25 mJ/m^2 according to (Nakano and Jacques, 2010), and the full dislocations tend to dissociate into Shockley partials and to generate wide SFs. Remy and Pineau (1977) and Allain et al. (2004) have summarized the relationships between the deformation mechanisms and SFE in high-Mn steels, and found that the ε-martensitic transformation dominates over SFE below 12 mJ/m^2. Recently, Pierce et al. (2015) confirmed this trend in various Fe-Mn-Al-Si alloys, but the critical SFE was found between 15 mJ/m^2 and 21 mJ/m^2. The finding in the present study is more consistent with Pierce's results.

The microscopic observations suggest that the ε-martensitic transformation proceeds by the gradual overlapping of SFs building up the nanometric FCC+HCP lamellar structure and finally the highly-faulted HCP phase (Fig. 7). The highly-faulted HCP phase cannot be explained by the pole mechanism, which predicts the formation of a perfect HCP plate (Bilby, 1953; Seeger, 1956). The model proposed by Fujita and Ueda (1972) emphasized the role of activating double slip systems in the generation and overlapping of wide SFs. The overlapping of SFs occurs irregularly at first and gradually changes into a regular sequence, providing an explanation for the formation of a faulted HCP structure. In this model, the multi-variant nature of the transformation is an intrinsic feature, which is contradictory to the present observation of a single variant of HCP plates in the ultrafine austenitic grains (Fig. 6).

There is a high density of pre-existing SFs in the ausformed UFG Fe23Mn alloys (Fig. 3). Thus, the generation and overlapping of wide SFs do not require the activation of a double-slip system as proposed in Fujita and Ueda (1972). During deformation, the pre-existing SFs with favored orientation expand along the primary slip plane, the overlapping of which form numerous thin HCP plates spanning through the lamellar austenitic grains. In addition, the high density of GBs in the UFG structure constitute possible dislocation sources, and SFs could directly emit from the GBs (Lai et al., 2020). Upon further deformation, the formation of SFs is sustained and the number of thin martensite plates keeps increasing. But, the widening of SFs along another slip system is prohibited by the existing SFs or HCP plates (Fig. 7e). The mutual impingement of the parallel ε-martensite plates leads to the FCC + HCP nanolamellar structure and finally to the faulted HCP region. Therefore, the main features of the deformation-induced ε-martensitic transformation, including the FCC+HCP nanolamellar, high SF density in HCP phase and single-variant nature, are closely linked to

the substructures and GBs introduced by the heavy ausforming.

4.3. Role of UFG ε-martensite on mechanical properties

The UFG Fe23Mn microstructure exhibits a significant strain hardening capacity, which is opposite to conventional UFG metals (Pineau et al., 2016). The superior strain hardening is attributed to the TRIP effect, i.e. the ε-martensitic transformation can occur by overcoming the strong mechanical constraint in the UFG structure (Ko et al., 2017); the ε-martensite is a stronger constituent than the austenite, and the progressive formation of ε-martensite enables a dynamic composite effect (Hatami et al., 2017; Lani et al., 2007; Li et al., 2017a; Xu et al., 2020). The efficiency of the TRIP effect depends on the transformation kinetics, the plastic compatibility between phases and also on the local responses of phases (Ennis et al., 2017; Ma and Hartmaier, 2015). As shown in Fig. 1, the lack of ductility of HCP ε-martensite at the CG state leads to the issue of premature failure. But microstructural refinement has a profound effect on the deformation mechanism and mechanical properties of ε-martensite. The plastic deformation of the UFG alloy is thus analyzed with a simple mean-field micromechanical model, with an emphasis on capturing the impact of the UFG ε-martensite. The stress and strain partitioning are described by an elementary rule of mixtures:

$$\sigma(\varepsilon) = \left[1 - V_f\right]\sigma_\gamma\left(\varepsilon_\gamma\right) + V_f\sigma_\varepsilon(\varepsilon_\varepsilon) \tag{4}$$

$$\varepsilon = \left[1 - V_f\right]\varepsilon_\gamma + V_f\varepsilon_\varepsilon \tag{5}$$

where V_f is the volume fraction of ε-martensite evolving with strain; σ_ε and σ_γ stand for the per phase stress in the ε-martensite and austenite, respectively; ε_ε and ε_γ are the per phase strain in the ε-martensite and austenite, respectively. A linear function is suggested for the transformation kinetics by fitting the data in Fig. 4c:

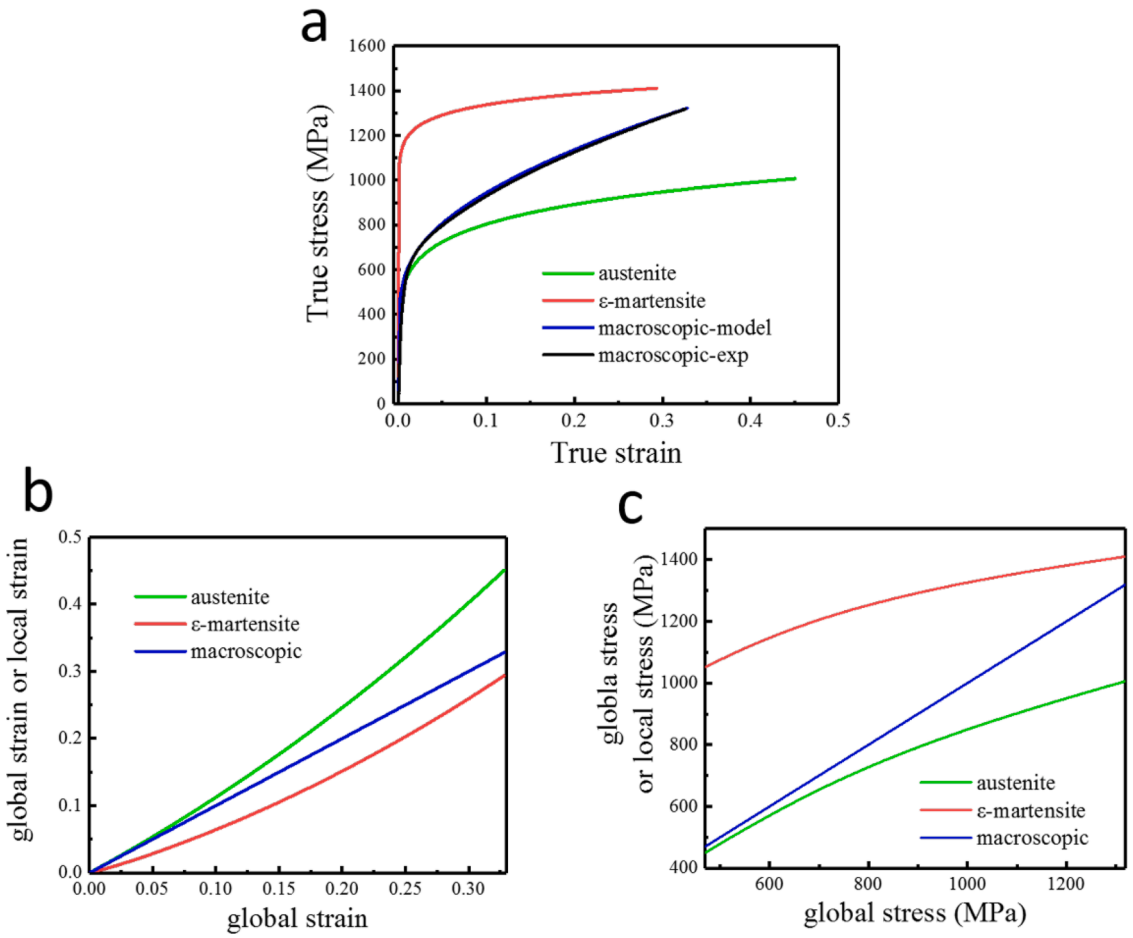

Fig.. 10. Micromechanical modeling of the tensile response of the UFG Fe-23Mn alloy. (a) The comparison of the experimental and simulated stress-strain curves, as well as the local stress-strain responses of austenite and ε-martensite; K_γ, K_ε, n_γ and n_ε are equal to 1135 MPa, 1500 MPa, 0.15 and 0.05, respectively. (b) and (c) Strain and stress partitioning, respectively.

$$V_f = 2.292\varepsilon + 0.028 \tag{6}$$

Thereafter, the iso-work assumption is adopted to model the mechanical response of a disordered two-phase structure (Bouaziz and Buessler, 2004). The mechanical response of dual-phase steels, quenching & partitioning steels and titanium alloys have been satisfactorily modeled by this approach (Bouaziz and Buessler, 2004; de Formanoir et al., 2019; Seo et al., 2016). Under the iso-work assumption, the incremental mechanical work is equal in both phases, which is intermediate between the iso-strain and iso-stress conditions. The stress and strain in austenite and ε-martensite follow the relationship of

$$\sigma_\gamma d\varepsilon_\gamma = \sigma_\varepsilon d\varepsilon_\varepsilon \tag{7}$$

It is assumed that both austenite and ε-martensite follow the Hollomon-type flow law, given by

$$\sigma_\gamma = K_\gamma \varepsilon^{n_\gamma} \tag{8}$$

$$\sigma_\varepsilon = K_\varepsilon \varepsilon^{n_\varepsilon} \tag{9}$$

where K_γ, K_ε, n_γ and n_ε are the fitting parameters. The initial single-phase UFG Fe23Mn microstructure justifies that the onset of plastic yielding is dictated by the response of the austenite, which sets the values of K_γ and n_γ. The parameters of the ε-martensite are identified using an inverse procedure by fitting the experimental true stress-true strain curve of UFG Fe23Mn. According to Fig. 10a, the macroscopic tensile curve can be satisfactorily reproduced by the model.

After identification, the UFG ε-martensite turns out to have a high yield strength, and is co-deforming with the austenite, attaining a per phase strain up to 0.3 as shown in Fig. 10a. The strain partitioning between austenite and ε-martensite is shown in Fig. 10b. Initially, the austenite phase is dominating the plastic deformation because of the negligible amount of ε-martensite; while at larger deformation, the local plastic strain in ε-martensite increases a lot, and becomes the main carrier of plastic deformation due to the high volume fraction. In terms of the stress partitioning (Fig. 10c), the UFG ε-martensite presents a much higher yield strength than the austenite, but the strain hardening is moderate when compared to the austenite phase. Therefore, the strength contrast between phases is large at the initial deformation and is reduced gradually with strain. The per phase stress in the UFG ε-martensite is close to the experimental fracture stress because the volume fraction of ε-martensite is high at large strains. Note that a variation of the fitting parameters will slightly change the per phase stress level in the ε-martensite, but the conclusions of the co-deformation and significant stress/strain partitioning remain unchanged. The strain hardening exponents of the individual phases, $n_\gamma = 0.15$ and $n_\varepsilon = 0.05$, are low values due to the UFG nature (Pineau et al., 2016), while the high macroscopic strain hardening exponent n comes from the TRIP effect.

As revealed by the micromechanical model, the strain hardening capacity of the UFG Fe23Mn alloy is attributed to the gradual formation of the stronger phase and the development of the internal stresses. The strength contrast between phases is the most pronounced at the small deformation. But the ε-martensite is plastically co-deforming with the austenite in UFG Fe23Mn, allowing large per phase plastic strain to build up. Generally speaking, a strong and elastically deforming second phase is most favorable to enhance the macroscopic strain hardening capacity (Lai et al., 2016). The yielding of the reinforcement will relax the internal stresses and decrease the strain hardening rate. But for the TRIP alloys, the gradual formation of the stronger phase, although plastically deforming as well, is also contributing to the continuous development of back stresses and thus to an efficient dynamic composite effect (Spencer et al., 2004). The significant stress partitioning as shown in Fig. 10c is demonstrating the development of internal stresses. This also indicates that the UFG ε-martensite can bear high stress levels without failure, which is in agreement with the experimental observation of the high macroscopic fracture stress of the UFG Fe23Mn alloy. In addition, both the experimental and modeling results consistently reveal that the UFG ε-martensite can carry significant plastic deformation as opposed to the brittleness of the CG microstructure. Therefore, reducing the grain size to an ultrafine scale has an important and positive impact on the mechanical properties of ε-martensite, which is the key microstructural origin of the excellent mechanical properties of UFG Fe23Mn.

In the polycrystalline HCP metals, mechanical twinning and the non-basal <c+a> slip are necessary mechanisms to accommodate the plastic strain in the <c> direction to maintain a generalized homogeneous plastic flow. The mechanical twinning involves the shear in the systems of $\{10\bar{1}2\}\langle 10\bar{1}\bar{1}\rangle$ and $\{10\bar{1}1\}\langle 10\bar{1}2\rangle$, while the <c+a> dislocations are activated in the slip system of $\{11\bar{2}2\}\langle 11\bar{2}\bar{3}\rangle$. Usually, the critical resolved shear stress for twinning is lower than that for the non-basal <c+a> slip (Agnew and Duygulu, 2005; Agnew et al., 2001), which explains the easier activation of twinning than <c+a> dislocations in the coarse-grained HCP metals. However, mechanical twinning could induce premature failure. A high stress concentration develops at the location of the twin-twin intersection or when the twin is blocked by a GB, which could be high enough to induce crack nucleation (Christian and Mahajan, 1995; Sree Harsha, 1981; Xiao et al., 2021; Yoo, 1981). It is also reported that the $\{10\bar{1}1\} - \{10\bar{1}2\}$ double twinning leads to strain localization and to the generation of twin-sized voids, resulting in shear failure at low strains (Barnett, 2007; Barnett et al., 2008). For the case of CG Fe23Mn alloy, microcracking induced by twinning is indeed observed (Fig. 1e). Therefore, if the high stress concentration is avoided by suppressing twinning, the fracture resistance of HCP metals should be improved. It is widely reported that the propensity of mechanical twinning in HCP metals is reduced when the grain size decreases (Ghaderi and Barnett, 2011; Koike et al., 2003; Luo et al., 2020; Zheng et al., 2020). The grain size effect is usually explained based on the Hall-Petch law; i.e. mechanical twinning involves a higher Hall-Petch slope than dislocation slip, and the twinning-slip transition occurs when the critical resolved shear stress for <c+a> dislocation slip is lower than that for twinning (Meyers et al., 2001). However, the statistical investigation in (Beyerlein et al., 2010) provides the important observation that the micro-sized grain diameter has generally no noticeable effect on whether or not the grain deforms by twinning; instead, the number of twins per grain decreases when reducing the grain size (Barnett,

2008; Beyerlein et al., 2010; Ghaderi and Barnett, 2011). The suppression of twinning and the predominant <c+a> slip become clear below certain critical grain size (Barnett et al., 2004; Luo et al., 2020). A recent dislocation dynamic simulation (Fan et al., 2016) reveals that twinning deformation is favored in larger grains but the plastic strain mediated by twin boundary migration in smaller grains is significantly smaller. The twin boundary migration becomes difficult due to the strong suppression of twinning dislocation activity by the smaller grain size. This could be attributed to the constraint from the surrounding neighboring grains which generates a backstress to hinder the twin boundary migration (Kumar et al., 2016). Therefore, the <c+a> dislocations, although with a larger magnitude of Burgers vector and a higher critical resolves shear stress, are activated by the higher yield stress due to grain refinement. Note that, in the present study, twinning in the UFG ε-martensite is suppressed both in number and size, and could be related to the high density of SFs in ε-martensite and the retained austenite domain, which impede the propagation of a twinning nuclei (Fig. 7d).

In HCP metals, the ductility can be improved by the activation of non-basal <c+a> slip (Agnew et al., 2002; 2001; Koike et al., 2003; Liu et al., 2019; Yoo, 1981). As emphasized by Yoo (1981), <c+a> slip is more effective in satisfying the compatibility conditions compared to the simultaneous activation of several twinning systems. Deformation by non-basal <c+a> slip does not involve a stress concentration at the tip of a twinning plate responsible for crack initiation. Therefore, the premature failure in the CG sample is avoided in the UFG ε-martensite, where twinning is suppressed and <c+a> dislocations are activated. The high density of dislocations with a <c> component (Fig. 8), the development of local misorientation and high density of LAGBs (Fig. 6) prove that the dislocation multiplication process is not limited in the UFG ε-martensite. In addition, the abundance of <c> dislocation segments is probably the result of the dissociation of <c+a> dislocations (Wu and Curtin, 2016). The <c+a> dislocations are glissile, while the <c> dislocations are sessile and are strong obstacles (Jones and Hutchinson, 1981; Wu and Curtin, 2016). The continuous generation of <c+a> dislocations increases the number of internal shear carriers to accommodate plastic strain, and the accompanying dissociation results in a multiplication of <c> dislocations (Wu and Curtin, 2016). In summary, the significant grain-size effect on the deformation behavior of ε-martensite enables an efficient stress partitioning and plastic co-deformation, which improves the strengthening and ductility efficiency of the strain-induced transforming structure.

5. Conclusions

The Fe-23 wt.%Mn alloy has been engineered by heavy ausforming, and a systematic study has been conducted to reveal the microstructure and mechanical performances, as well as to unravel the underlying deformation mechanisms as a function of grain size. The main conclusions are as follows:

1 The ausforming with 90% rolling reduction produces an UFG microstructure, which is observed to fully suppress the ε-martensitic transformation and to stabilize the austenite phase at RT, in contrast with the CG counterpart, which exhibits 65 vol.% ε-martensite.
2 The UFG Fe23Mn microstructure presents a high combination of strength, uniform elongation and fracture strain, hence resisting both plastic localization and damage accumulation. The high ductility of the heavily-ausformed Fe23Mn alloy with no subsequent annealing step contradicts the general trend of UFG alloys produced by severe plastic deformation.
3 The UFG Fe23Mn microstructure presents a sustained high strain hardening rate, leading to a postponed necking. Such enhanced strain hardening capacity is attributed to the deformation-induced ε-martensitic transformation (the TRIP effect).
4 The ε-martensite is found to deform plastically up to large strain which is opposite to the conventional HCP response. This appears to come from the suppression of mechanical twinning at the expense of abundant non-basal <c+a> slip activation.
5 As a result, the UFG microstructure fails in a ductile mode with improved resistance to damage initiation as compared to the brittleness of the CG counterpart. Premature failure is avoided and this suggests that non-basal <c+a> slip involves less local stress concentration compared to twinning.
6 A significant stress/strain partitioning in the transformable microstructure and the large co-deformation of the UFG ε-martensite are predicted by an elementary micromechanical model under the isowork assumption.

Consequently, this work inspires exploring the potential of a metastable alloy relying on engineering the prior austenitic microstructure, which significantly influences the phase content and deformation mechanisms.

CRediT authorship contribution statement

Qingquan Lai: Conceptualization, Methodology, Investigation, Writing – review & editing, Supervision. **Huiqin Yang:** Visualization, Methodology, Investigation. **Yuntao Wei:** Visualization. **Hao Zhou:** Formal analysis. **Lirong Xiao:** Formal analysis. **Huiqiang Ying:** Resources, Formal analysis. **Si Lan:** Resources, Formal analysis. **Zesheng You:** Resources, Methodology. **Zongde Kou:** Resources, Methodology, Formal analysis. **Tao Feng:** Resources, Investigation, Writing – review & editing. **Qi Lu:** Resources, Investigation, Writing – review & editing. **Pascal Jacques:** Methodology, Investigation, Writing – review & editing. **Thomas Pardoen:** Supervision, Writing – review & editing.

Declaration of Competing Interest

The authors declare that they have no known competing financial interests or personal relationships that could have appeared to influence the work reported in this paper.

Acknowledgments

This study is supported by the National Key R&D Program of China (Grant No. 2017YFA0204403), the National Natural Science Foundation of China (Nos. 55001166, 51871120), the Natural Science Foundation of Jiangsu Province (Grant No. BK20180492) and the Fundamental Research Funds for the Central Universities (Grant nos. 30920021158, 30920010004). We acknowledge the use of the resources of the China Spallation Neutron Source in Dongguan of Guangdong Province of P. R. China and are grateful to Dr. Hualen He for the assistance in neutron diffraction experiments. The helpful discussion with Prof. Ke Lu at SYNL-IMR is greatly appreciated.

Supplementary materials

Supplementary material associated with this article can be found, in the online version, at doi:10.1016/j.ijplas.2021.103151.

References

Agnew, S.R., Duygulu, O., 2005. Plastic anisotropy and the role of non-basal slip in magnesium alloy AZ31B. Int. J. Plast. 21, 1161–1193.
Agnew, S.R., Horton, J.A., Yoo, M.H., 2002. Transmission electron microscopy investigation of < c+a >dislocations in Mg and alpha-solid solution Mg-Li alloys. Metall. Mater. Trans. A 33, 851–858.
Agnew, S.R., Yoo, M.H., Tome, C.N., 2001. Application of texture simulation to understanding mechanical behavior of Mg and solid solution alloys containing Li or Y. Acta Mater. 49, 4277–4289.
Allain, S., Chateau, J.P., Bouaziz, O., Migot, S., Guelton, N., 2004. Correlations between the calculated stacking fault energy and the plasticity mechanisms in Fe-Mn-C alloys. Mater. Sci. Eng. A 387, 158–162.
Barnett, M.R., 2007. Twinning and the ductility of magnesium alloys Part II. "Contraction" twins. Mater. Sci. Eng. A 464, 8–16.
Barnett, M.R., 2008. A rationale for the strong dependence of mechanical twinning on grain size. Scr. Mater. 59, 696–698.
Barnett, M.R., Jacob, S., Gerard, B.F., Mullins, J.G., 2008. Necking and failure at low strains in a coarse-grained wrought Mg alloy. Scr. Mater. 59, 1035–1038.
Barnett, M.R., Keshavarz, Z., Beer, A.G., Atwell, D., 2004. Influence of grain size on the compressive deformation of wrought Mg-3Al-1Zn. Acta Mater. 52, 5093–5103.
Beyerlein, I.J., Capolungo, L., Marshall, P.E., McCabe, R.J., Tome, C.N., 2010. Statistical analyses of deformation twinning in magnesium. Philos. Mag. 90, 2161–2190.
Bilby, B.A., 1953. On the mutual transformation of lattices. Philos. Mag. 44, 782–785.
Bouaziz, O., Allain, S., Scott, C.P., Cugy, P., Barbier, D., 2011. High manganese austenitic twinning induced plasticity steels: a review of the microstructure properties relationships. Curr. Opin. Solid State Mater. Sci. 15, 141–168.
Bouaziz, O., Buessler, P., 2004. Iso-work increment assumption for heterogeneous material behavior modelling. Adv. Eng. Mater. 6, 79–83.
Bouaziz, O., Guelton, N., 2001. Modelling of TWIP effect on work-hardening. Mater. Sci. Eng. A 319, 246–249.
Bu, Y., Li, Z., Liu, J., Wang, H., Raabe, D., Yang, W., 2019. Nonbasal slip systems enable a strong and ductile hexagonal-close-packed high-entropy phase. Phys. Rev. Lett. 122, 075502.
Cao, Y., Ni, S., Liao, X., Song, M., Zhu, Y., 2018. Structural evolutions of metallic materials processed by severe plastic deformation. Mater. Sci. Eng. R 133, 1–59.
Chowdhury, P., Canadinc, D., Sehitoglu, H., 2017. On deformation behavior of Fe-Mn based structural alloys. Mater. Sci. Eng. R 122, 1–28.
Christian, J.W., Mahajan, S., 1995. Deformation twinning. Prog. Mater. Sci. 39, 1–57.
De Cooman, B.C., Estrin, Y., Kim, S.K., 2018. Twinning-induced plasticity (TWIP) steels. Acta Mater. 142, 283–362.
de Formanoir, C., Martin, G., Prima, F., Allain, S.Y.P., Dessolier, T., Sun, F., Vives, S., Hary, B., Brechet, Y., Godet, S., 2019. Micromechanical behavior and thermal stability of a dual-phase α+α' titanium alloy produced by additive manufacturing. Acta Mater. 162, 149–162.
Ennis, B.L., Jimenez-Melero, E., Atzema, E.H., Krugla, M., Azeem, M.A., Rowley, D., Daisenberger, D., Hanlon, D.N., Lee, P.D., 2017. Metastable austenite driven work-hardening behaviour in a TRIP-assisted dual phase steel. Int. J. Plast. 88, 126–139.
Fabregue, D., Pardoen, T., 2008. A constitutive model for elastoplastic solids containing primary and secondary voids. J. Mech. Phys. Solids 56, 719–741.
Fan, H., Aubry, S., Arsenlis, A., El-Awady, J.A., 2016. Grain size effects on dislocation and twinning mediated plasticity in magnesium. Scr. Mater. 112, 50–53.
Fujita, H., Ueda, S., 1972. Stacking faults and F.C.C. (γ)-H.C.P. (ε) transformation in 18/8 type stainless steel. Acta Metall. 20, 759–767.
Ghaderi, A., Barnett, M.R., 2011. Sensitivity of deformation twinning to grain size in titanium and magnesium. Acta Mater. 59, 7824–7839.
Gil Sevillano, J., de las Cuevas, F., 2019. A comparison of the internal stresses in a transformation-induced plasticity-assisted steel and a twinning-induced plasticity steel. Mater. Sci. Technol. 35, 409–419.
Gong, W., Tomota, Y., Adachi, Y., Paradowska, A.M., Kelleher, J.F., Zhang, S.Y., 2013. Effects of ausforming temperature on bainite transformation, microstructure and variant selection in nanobainite steel. Acta Mater. 61, 4142–4154.
Grassel, O., Kruger, L., Frommeyer, G., Meyer, L.W., 2000. High strength Fe-Mn-(Al, Si) TRIP/TWIP steels development - properties - application. Int. J. Plast. 16, 1391–1409.
Hatami, M.K., Pardoen, T., Lacroix, G., Berke, P., Jacques, P.J., Massart, T.J., 2017. Towards ultra-high ductility TRIP-assisted multiphase steels controlled by strain gradient plasticity effects. J. Mech. Phys. Solids 98, 201–221.
Howe, J.M., Pond, R.C., Hirth, J.P., 2009. The role of disconnections in phase transformations. Prog. Mater. Sci. 54, 792–839.
Jones, I.P., Hutchinson, W.B., 1981. Stress-state dependence of slip in titanium-6Al-4V and other H.C.P. metals. Acta Metall. 29, 951–968.
Kim, J.K., De Cooman, B.C., 2017. Observation of dislocations with a Burgers vector containing a < c >component in martensitic hcp epsilon Fe-17%Mn. Scr. Mater. 128, 78–82.
Ko, W.S., Maisel, S.B., Grabowski, B., Jeon, J.B., Neugebauer, J., 2017. Atomic scale processes of phase transformations in nanocrystalline NiTi shape-memory alloys. Acta Mater. 123, 90–101.
Koike, J., Kobayashi, T., Mukai, T., Watanabe, H., Suzuki, M., Maruyama, K., Higashi, K., 2003. The activity of non-basal slip systems and dynamic recovery at room temperature in fine-grained AZ31B magnesium alloys. Acta Mater. 51, 2055–2065.
Koyama, M., Kaneko, T., Sawaguchi, T., Tsuzaki, K., 2018. Microstructural damage evolution and arrest in binary Fe-high-Mn alloys with different deformation temperatures. Int. J. Fract. 213, 193–206.
Koyama, M., Sawaguchi, T., Tsuzaki, K., 2012. Premature fracture mechanism in an Fe-Mn-C austenitic steel. Metall. Mater. Trans. A 43, 4063–4074.
Kumar, M.A., Beyerlein, I.J., Tome, C.N., 2016. Grain size constraints on twin expansion in hexagonal close packed crystals. J. Appl. Phys. 120, 155105.
Lai, Q., Brassart, L., Bouaziz, O., Goune, M., Verdier, M., Parry, G., Perlade, A., Brechet, Y., Pardoen, T., 2016. Influence of martensite volume fraction and hardness on the plastic behavior of dual-phase steels: experiments and micromechanical modeling. Int. J. Plast. 80, 187–203.
Lai, Q., Song, P., Zhou, H., Xiao, L., Feng, T., Li, C., 2020. Deformation-induced martensitic transformation and strain hardening in a nanocrystalline FeMn alloy processed by severe austenite pre-deformation. Materialia 13, 100832.
Lani, F., Furnemont, Q., Van Rompaey, T., Delannay, F., Jacques, P.J., Pardoen, T., 2007. Multiscale mechanics of TRIP-assisted multiphase steels: II. Micromechanical modelling. Acta Mater. 55, 3695–3705.

Li, Y., Li, W., Hu, J.C., Song, H.M., Jin, X.J., 2017a. Compatible strain evolution in two phases due to epsilon martensite transformation in duplex TRIP-assisted stainless steels with high hydrogen embrittlement resistance. Int. J. Plast. 88, 53–69.
Li, Z., Tasan, C.C., Pradeep, K.G., Raabe, D., 2017b. A TRIP-assisted dual-phase high-entropy alloy: grain size and phase fraction effects on deformation behavior. Acta Mater. 131, 323–335.
Li, Z.M., Pradeep, K.G., Deng, Y., Raabe, D., Tasan, C.C., 2016. Metastable high-entropy dual-phase alloys overcome the strength-ductility trade-off. Nature 534, 227–230.
Liang, X., McDermid, J.R., Bouaziz, O., Wang, X., Embury, J.D., Zurob, H.S., 2009. Microstructural evolution and strain hardening of Fe-24Mn and Fe-30Mn alloys during tensile deformation. Acta Mater. 57, 3978–3988.
Liu, B.Y., Liu, F., Yang, N., Zhai, X.B., Zhang, L., Yang, Y., Li, B., Li, J., Ma, E., Nie, J.F., Shan, Z.W., 2019. Large plasticity in magnesium mediated by pyramidal dislocations. Science 365, 73–75.
Luo, X., Feng, Z., Yu, T., Luo, J., Huang, T., Wu, G., Hansen, N., Huang, X., 2020. Transitions in mechanical behavior and in deformation mechanisms enhance the strength and ductility of Mg-3Gd. Acta Mater. 183, 398–407.
Ma, A., Hartmaier, A., 2015. A study of deformation and phase transformation coupling for TRIP-assisted steels. Int. J. Plast. 64, 40–55.
Madivala, M., Schwedt, A., Wong, S.L., Roters, F., Prahl, U., Bleck, W., 2018. Temperature dependent strain hardening and fracture behavior of TWIP steel. Int. J. Plast. 104, 80–103.
Meyers, M.A., Vohringer, O., Lubarda, V.A., 2001. The onset of twinning in metals: a constitutive description. Acta Mater. 49, 4025–4039.
Nakano, J., Jacques, P.J., 2010. Effects of the thermodynamic parameters of the hcp phase on the stacking fault energy calculations in the Fe-Mn and Fe-Mn-C systems. Calphad 34, 167–175.
Nishiyama, Z., 1978. Martensitic Transformation. Academic Press, New York.
Olson, G.B., Cohen, M., 1976. A general mechanism of martensitic nucleation. I. General concepts and the FCC-HCP transformation. Metall. Trans. A 7, 1897–1904.
Pierce, D.T., Jimenez, J.A., Bentley, J., Raabe, D., Wittig, J.E., 2015. The influence of stacking fault energy on the microstructural and strainhardening evolution of Fe-Mn-Al-Si steels during tensile deformation. Acta Mater. 100, 178–190.
Pineau, A., Benzerga, A.A., Pardoen, T., 2016. Failure of metals III: fracture and fatigue of nanostructured metallic materials. Acta Mater. 107, 508–544.
Remy, L., Pineau, A., 1977. Twinning and strain-induced FCC-HCP transformation in the Fe-Mn-Cr-C system. Mater. Sci. Eng. 28, 99–107.
Schuman, V.H., 1972. Martensitische Umwandlung in austenitischen Mangan-Kohlenstoff-Stählen. Neue Hütte 17, 605–609.
Seeger, A., 1956. Dislocations and allotropic transformations II. Z. Metallk. 47, 653–660.
Seo, E.J., Cho, L., Estrin, Y., De Cooman, B.C., 2016. Microstructure-mechanical properties relationships for quenching and partitioning (Q&P) processed steel. Acta Mater. 113, 124–139.
Sevillano, J.G., 2009. An alternative model for the strain hardening of FCC alloys that twin, validated for twinning-induced plasticity steel. Scr. Mater. 60, 336–339.
Sipos, K., Remy, L., Pineau, A., 1976. Influence of austenite predeformation on mechanical properties and strain-induced martensitic transformations of a high manganese steel. Metall. Trans. A 7, 857–864.
Spencer, K., Embury, J.D., Conlon, K.T., Veron, M., Brechet, Y., 2004. Strengthening via the formation of strain-induced martensite in stainless steels. Mater. Sci. Eng. A 387, 873–881.
Sree Harsha, K.S., 1981. Stress concentration of terminating twins. Metall. Trans. A 12, 365–370.
Su, J., Raabe, D., Li, Z., 2019. Hierarchical microstructure design to tune the mechanical behavior of an interstitial TRIP-TWIP high-entropy alloy. Acta Mater. 163, 40–54.
Takaki, S., Nakatsu, H., Tokunaga, Y., 1993. Effects of austenite grain size on epsilon martensitic transformation in Fe-15mass% Mn alloy. Mater. Trans. JIM 34, 489–495.
Tomota, Y., Strum, M., Morris, J.W., 1988. Tensile deformation behavior of mechanically stabilized Fe-Mn austenite. Metall. Trans. A 19, 1563–1568.
Tsuzaki, K., Fukasaku, S., Tomota, Y., Maki, T., 1991. Effect of prior deformation of austenite on the gammararrepsilon martensitic transformation in Fe-Mn alloys. Mater. Trans. JIM 32, 222–228.
Ungar, T., 2001. Dislocation densities, arrangements and character from X-ray diffraction experiments. Mater. Sci. Eng. A 309, 14–22.
Waitz, T., Tsuchiya, K., Antretter, T., Fischer, F.D., 2009. Phase transformations of nanocrystalline martensitic materials. MRS Bull. 34, 814–821.
Wang, H., You, Z., Lu, L., 2018. Kinematic and isotropic strain hardening in copper with highly aligned nanoscale twins. Mater. Res. Lett. 6, 333–338.
Wei, S., Kim, J., Tasan, C.C., 2019. Boundary micro-cracking in metastable Fe45Mn35Co10Cr10 high-entropy alloys. Acta Mater. 168, 76–86.
Wu, Z., Ahmad, R., Yin, B., Sandloebes, S., Curtin, W.A., 2018. Mechanistic origin and prediction of enhanced ductility in magnesium alloys. Science 359, 447–451.
Wu, Z., Curtin, W.A., 2016. Intrinsic structural transitions of the pyramidal I < c + a >dislocation in magnesium. Scr. Mater. 116, 104–107.
Xiao, J.F., Shang, X.K., Hou, J.H., Li, Y., He, B.B., 2021. Role of stress-induced martensite on damage behavior in a metastable titanium alloy. Int. J. Plast. 146, 103103.
Xu, S.S., Li, J.P., Cui, Y., Zhang, Y., Sun, L.X., Li, J., Luan, J.H., Jiao, Z.B., Wang, X.L., Liu, C.T., Zhang, Z.W., 2020. Mechanical properties and deformation mechanisms of a novel austenite-martensite dual phase steel. Int. J. Plast. 128.
Yoo, M.H., 1981. Slip, twinning, and fracture in hexagonal close-packed metals. Metall. Trans. A 12, 409–418.
Yoo, M.H., Morris, J.R., Ho, K.M., Agnew, S.R., 2002. Nonbasal deformation modes of HCP metals and alloys: role of dislocation source and mobility. Metall. Mater. Trans. A 33, 813–822.
Zheng, R., Du, J.-P., Gao, S., Somekawa, H., Ogata, S., Tsuji, N., 2020. Transition of dominant deformation mode in bulk polycrystalline pure Mg by ultra-grain refinement down to sub-micrometer. Acta Mater. 198, 35–46.